The conductive three dimensional topological structure enhanced magnetorheological elastomer towards a strain sensor

Lin Ge, Xinglong Gong[*], Yu Wang, Shouhu Xuan

CAS Key Laboratory of Mechanical Behavior and Design of Materials, Department of Modern Mechanics, University of Science and Technological of China, Hefei, 230027, China

ABSTRACT

Conductive magnetorheological elastomers (MREs) consisting of carbonyl iron particles (CIPs), poly-dimethylsiloxane matrix and carbon nanotube (CNT) covered polyurethane sponge (PUS) were developed. The CIPs were linearly orientated within the porous PUS and the magnetic saturation modulus of PUS-reinforced anisotropic MRE was 1.3 MPa when CIPs content was 70 wt%. This MRE presented typical magnetorheological (MR) effects and the shear storage modulus increased from 0.49 MPa to 0.64 MPa after reinforcing the anisotropic MRE with PUS. Owing to the presence of the CNTs on the PUS networks, the final MRE was conductive. The electrical resistance of the MRE increased with increasing tensile strain, ranging from 27.5 kΩ to 30.5 kΩ at various tensile rates (50, 100, 150, 200, 250 and 300 mm/min respectively). As a result, the smart MRE was effective in a flexible, sensitive and reversible strain sensor.

© 2016 Elsevier Ltd. All rights reserved.

1. Introduction

Because of their reversibly switching rheological properties under an external magnetic field, magnetorheological elastomers (MREs) have attracted great interest for a broad range of applications in architecture, vibration control, noise reduction, automotive industry, suspension system, bushings, absorbers etc. [1–6]. MREs are mainly fabricated by exposing mixtures of polymer matrix and soft magnetic particles to a magnetic field. The soft magnetic particles become oriented along the magnetic field direction and form linear structures. Over the past decade, various studies have been done to improve the mechanical properties of MRE, however, there are few studies on the development of novel applications using MREs.

Flexible, highly sensitive and low-cost tensile sensors were highly desirable in portable and foldable devices [7–9]. Very recently, it was found that the flexible tensile sensor-integrated MREs could generate signals to reflect the strength of tensile strain imposed on the MRE-based devices. This characteristic is very important in MRE application because these devices could identify the mechanical state of the MRE component. To this end, several flexible tensile and pressure magnetorheological (MR)

sensors had been fabricated. Huang et al. enhanced the electrical properties of magnetorheological fluid (MRF) by coating silver on CIPs. The enhanced electrical properties open a new way to realize the electrical control of MRF [10]. Tian et al. investigated the sensing capabilities of graphite-based MRE experimentally and theoretically. The graphite MREs showed a resistance change when an external load is applied to the MRE sample. Using this feather of MREs, the external stress signal can be converted to a resistance signal, which can potentially be used in a force sensor [11]. Unfortunately, the manufacture of these flexible sensors were complicated and expensive, thus their practical application was limited. Moreover, although these newly developed conductive MREs have been used as flexible conductors and strain sensors, their resistance sensitivity to the displacement was not stable.

Over the past decade, three-dimensional (3D) porous-geometry materials have been introduced to many smart materials to enhance the mechanical properties [12]. Plastomers, elastomers and tissues incorporated with 3D geometry scaffolds have been used in sandwich beam [13], tissue engineering [14], conductive applications [15,16] and so on. Polyurethane sponges (PUSs) are a typical commercially available 3D porous polymer with low density, high porosity, high absorption ability and good elasticity [17]. Integrating spontaneous and non-spontaneous orientation-ordered materials such as nematic liquid crystals, ferromagnetic, ferroelectric materials in devices based on porous structure such as PUS had been a subject of considerable research recent years

[18—21]. These previous work indicated that the MR effects of the MR plastomer could be enhanced by introducing the 3D PUS. These use of 3D PUSs offers many other advantages, such as porous [22], strong continuous absorption [23,24], significant internal surface area [25], good biocompatibility [26,27].

Furthermore, the inter-connective network of the 3D porous geometric material is effective in forming conductive routes in the materials. Therefore, the materials with this conductive 3D porous geometry such as zeolites [28], wool fibers [29] and sponges [30] have been applied to the fabrication of sensors owing to their combinational electronic conductivities and mechanical flexibilities. Combing the conductive 3D porous geometry with traditional MREs may result in a conductive MRE with good mechanical properties and high electronic conductivities. To this end, the development of conductive 3D porous network-strengthened MREs would attract special interest not only because of their fundamental significance but also because of their practical applications.

In this study, a conductive PUS was incorporated into a carbonyl iron particle (CIP)-doped polydimethylsiloxane (PDMS) matrix to develop a novel strain-sensitive MRE. The MRE exhibited good dynamic properties because the 3D continuous porous sponge strengthened the inner structure. The influences of magnetic field and CIP content on the mechanical properties were investigated. The MR effect of the MRE was analyzed and the formation mechanism is discussed and this simple fabrication method provides a possible method for fabricating highly sensitive and low-cost strain sensors.

2. Materials and methods

2.1. Materials

The PDMS precursor and curing agent (Sylgard 184) purchased from Dow Corning GmbH, USA was used as the MRE matrix. Commercially available PUS with continuous porous structure and smooth surface was used to confine the magnetic particles in MREs. The soft magnetic particles were CIPs, which were provided by BASF in Germany with an average diameter of 7 μm. A mold with dimensions of 50 mm $\times$ 50 mm $\times$ 1 mm was used to shape the MRE.

2.2. Preparation

Conductive PUS: A porous PUS with high conductivity was constructed by dip-coating carbon nanotubes (CNTs) onto the backbone of the PUS. Specifically, the PUS was cut to 20 mm in diameter and 1 mm in thickness. The bare PUS was immersed into the 1.2 mg/ml CNT ink prepared according to our previous work [31] and dried in an oven for 30 min.

Conductive MRE: 20 g silicon base, 1 g curing agent and 49 g CIPs (70 wt%) were mixed together in a beaker. The mixture was stirred for 10 min to ensure that the CIPs had been dispersed homogeneously in the silicon elastomers. The conductive PUS with its porous structure was immersed into the MR precursor. After that, the beaker containing the MR precursor and conductive PUS was transferred into a vacuum oven and pumped for 30 min to ensure that the conductive PUS was filled with the MR precursor under the capillary action. Then, the conductive PUS filled with the MR precursor was transferred into a 50 mm $\times$ 50 mm $\times$ 1 mm mold and heated for 20 min at 100 °C under 1 T magnetic field to ensure that the silicon elastomer was totally cross-linked. After that, the MREs were stored at room temperature for 72 h. The MRE containing conductive PUS was easily recognized and then cut out with a knife. The final diameter and the thickness of MREs were the same as the conductive PUS which was also 20 mm in diameter and 1 mm in thickness. Samples with CIP weight concentrations of 40 wt%, 60 wt %, 70 wt% and 80 wt% were fabricated. To investigate the topological confinement of CIPs in the continuous porous structures, MRE samples with pure PUS and without PUS were also fabricated.

Strain sensor: A porous PUS with high conductivity was prepared by dip-coating CNTs onto the backbone of the PUS. The size of the conductive PUS was 2 mm $\times$ 20 mm $\times$ 60 mm. Copper wire was connected to the conductive PUS with the conductive silver adhesives. The conductive PUS was immersed into the MR precursor with 70% CIPs content. After that, the beaker containing the MR precursor and conductive PUS was transferred into a vacuum oven and pumped for 30 min. Then conductive PUS filled with MR precursor was transferred to a 100 mm $\times$ 100 mm $\times$ 2 mm mold and the rest of the space was filled with pure MR precursor. The mold was heated for 20 min at 100 °C. Finally, a strain sensor with size of 2 mm $\times$ 20 mm $\times$ 60 mm was obtained.

2.3. Characterization

An environment scanning electron microscope (SEM, Philips of Holland, model XT30 ESEM-MP) was used to observe the microstructure of the MREs and the PUS. The accelerating voltage was 20 kV. These samples were cut into sheets and coated with thin layer of gold prior to SEM observation.

Synchrotron radiation X-ray computed tomography (SR-CT) experiments performed on BL13W1 beam line in Shanghai synchrotron radiation facility (SSRF) were used to observe the 3D network in MREs [32]. The synchrotron radiation X-ray passed through the samples and were recorded by a Charge-coupled Device camera (14 bit dynamic, 2048 $\times$ 2048 pixel array) at a distance of 14 cm from the samples. The sample was imaged in protection at a regular increment from 0° to 180°, each with 720 radiographs with an exposure time of 1 s and a beam energy of 15 keV. The reconstructed 3D structures were obtained by analyzing the projection images with a filtered back-projection algorithm.

The rheological properties of topological confined MREs were measured by a rheometer (Physica MCR 301, Anton Paar Co., Austria). The samples were placed between the paralleled rotating disc and the base. An electromagnetic coil was used to generate a magnetic field strength by applying current to it. Magnetic field strengths ranged from 0 mT to 1000 mT was achieved by adjusting the coil current from 0 A to 5 A. The test was undertaken in shear oscillation mode. The frequency was 5 Hz and the strain amplitude was 0.1%. The temperature was 25 °C.

The cycle tensile loading test on the sample and the tensile strength were tested by Material Test System (MTS) (MTS criterion 43, MTS System Co., America). The sample size was 2 mm $\times$ 20 mm $\times$ 60 mm. Modulab® material system (Solartron analytical, AMETEK advanced measurement technology, Inc., United Kingdom) and data storage and analyzing system (Softwere) were used to test the resistance. A 2 mm $\times$ 20 mm $\times$ 10 mm area of the sample on each side was fixed onto the MTS with a clamp. Thus, the testing area was 2 mm $\times$ 20 mm $\times$ 40 mm. The tensile rate was 1 mm/min and the tensile rates of cycle tensile loading test on the strain sensor were 50, 100, 150, 200, 250 and 300 mm/min. At the same time, a copper wire was connected the sample and the electric conductivity was tested by the Modulab® material system, which supplied direct voltage excitation and measured the responsive current. Finally, the current data was collected in the data storage and analysis system.

3. Results and discussion

In this work, four kinds of MREs with different weight fractions of CIPs were fabricated. For MREs with certain weight fraction of

CIPs, the CIPs dispersed in two different ways: 1) The CIPs in the isotropic PUS-MRE were spread randomly and homogeneously in the matrix (denoted as I-PUS-MRE). 2) The CIPs in anisotropic PUS-MRE were assembled in the MRE matrix by forming linear structure (denoted as A-PUS-MRE). The A-PUS-MRE was achieved by applying a 1 T magnetic field (100 °C, 20 min) on the MRE precursor incorporated PUS during the curing process. The CIPs were re-assembled to form a linear structure owing to the magnetic forces.

SEM and SR-CT were used to investigate the porous structure of PUS and the microstructure of PUS-MRE. Fig. 1(a) was the SEM image of the PUS. The porous structure of the PUS helped confining the CIPs, thus strengthening the local CIP ordering. The cross section of the MRE matrix was shown in Fig. 1(b) and the raised surface was the bone structure of PUS/CNT, which was filled with pure PDMS elastomer. Fig. 1(c) shows the microstructure of I-PUS/CNT-MRE. It can be seen that the CIPs were spread randomly and homogeneously in the matrix. The white triangular bulge was

estimated to be the PUS because it exhibited the structural characteristics. Fig. 1(d) shows the SEM image of the A-PUS/CNT -MRE. Clearly, the CIPs assembled to form linear structure under a magnetic field within the PDMS matrix. The green arrow in Fig. 1(d) represents the CIPs aligned in the direction of the magnetic field.

SR-CT was used to observe the inner 3D alignment structure in A-PUS/CNT-MRE. As shown in Fig. 1(e) and (f), SR-CT provides 3D information on the microstructure by the reconstructing multiple 2D images with 0.7 μm pixel size under different angles of view. Both the PUS and the PDMS elastomer were weak X-ray absorption materials and had similar X-ray absorption coefficients. The CIPs were strong X-ray absorption material, and therefore it would be easy to obtain clear reconstruction images of CIPs alignment in A-PUS/CNT-MRE. For simplicity, the images show only the CIP morphological structure after removing the PDMS elastomer and PUS matrix by image filtering. As shown in the resulting side-view image, the CIPs were confined in the PUS, forming a linear structure
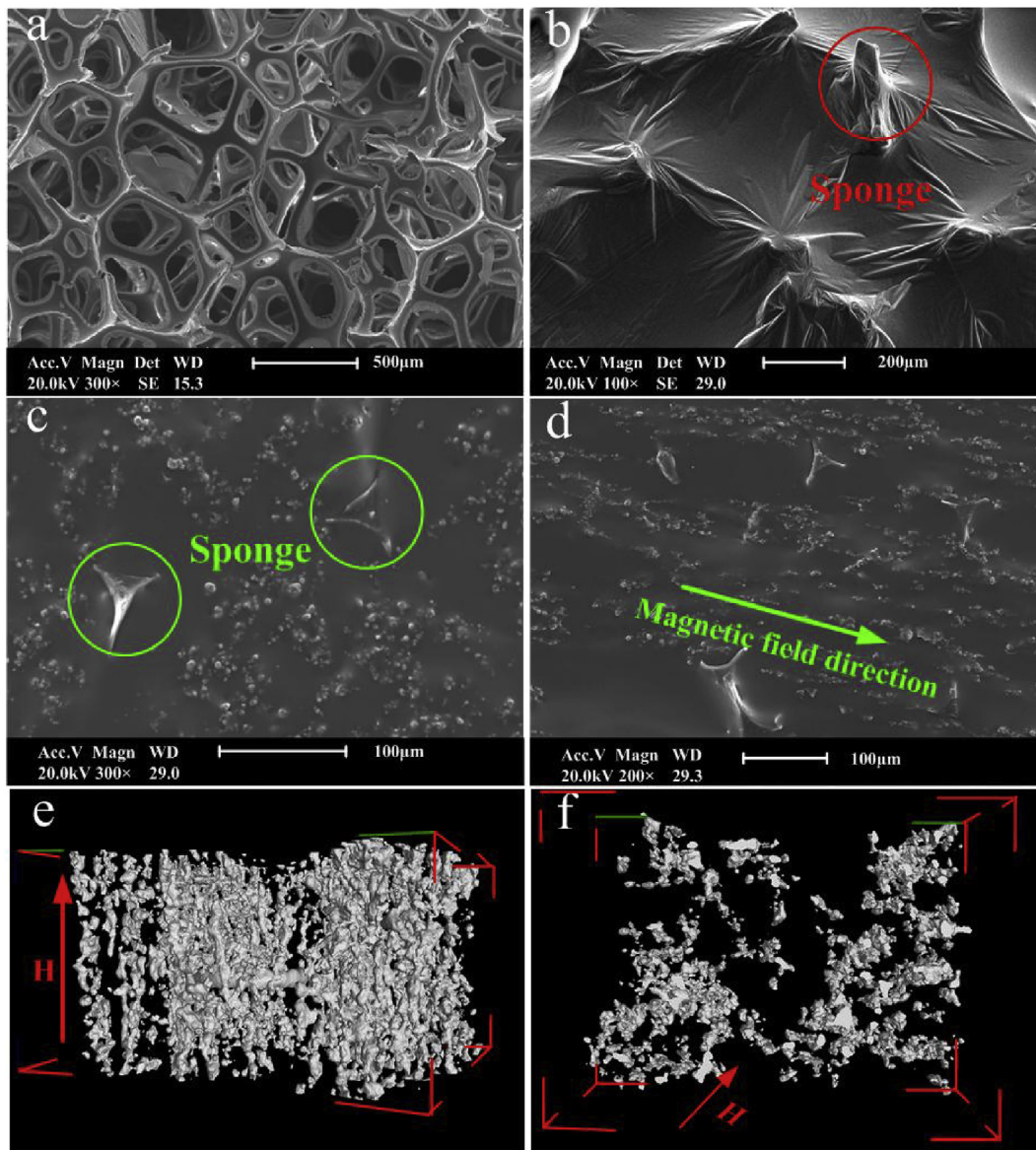

Fig. 1. SEM images of PUS and MREs (a) SEM image of porous PUS (b) SEM image of MRE matrix formed by PDMS and PUS/CNT (c) SEM image of I-MREs with PUS/CNT (I-PUS/CNT-MRE) microstructure (d) SEM image of A-MREs PUS/CNT (A-PUS/CNT-MRE) microstructure (e) SR-CT 3D reconstruction image of CIPs chains in the A-PUS/CNT-MRE viewed from the side (f) SR-CT 3D reconstruction image of CIPs chains in the A-PUS/CNT-MRE viewed from top down.

in the direction of the magnetic field because the PUS limited the interaction between the CIPs. The linear structure was more clearly in the top view. The CIPs were aggregated together, and the blank spaces between the linear structures were occupied by polymer.

The magnetic field played a very important role on the CIP distribution in the MRE. The CIPs were confined in the porous structures and anchored by PDMS molecular chains to the pore surface of PUS/CNT. The CIPs spread randomly in the porous structure in I-PUS/CNT-MREs. During the preparation, when an external magnetic field was applied to the MRE precursor, the CIPs were propelled by dipole magnetic force to form linear structure paralleled to the magnetic field. Then, cross-linking anchored the linear structure within the pores of PUS/CNT. Here, the anchoring also strengthened the linear structure in the MREs.

3.1. Dynamic properties of the topological confined MREs

The influence of CIPs on MRE shear storage modulus (G') under different magnetic field flux densities B was shown in Fig. 2(a). The weight fraction of CIPs in MREs was 70%. G' increased with increasing of the magnetic flux density before the soft magnetic CIPs were saturated by the excessively strong field. The PUS therefore played a very important role on G' value. The sample with

highest magnetic induced modulus ($\Delta G'$) was A-PUS-MRE, with a value of 0.64 MPa. Meanwhile, the sample with the lowest $\Delta G'$ was I-MRE, which had a value of 0.28 MPa. For the A-PUS-MRE, the magnetic saturation modulus (G_{max}') was 1.30 MPa (Table 1), which was much higher than that of A-MRE (0.96 MPa). For I-PUS-MRE, the G_{max}' (0.73 MPa) was much higher than that of I-MRE (0.52 MPa). As compared to the MRE without PUS, the initial storage modulus (G_0') of the A-PUS-MRE was as high as 0.66 MPa, whereas that of I-PUS-MRE was the lowest, 0.21 MPa.

The continuous porous structure also influenced the MR effect. The MR effects of I-PUS-MRE and A-PUS-MRE were 248% and 97%, respectively. However, the MR effects of I-MRE and A-MRE was 117% and 104%, respectively. I-PUS-MRE thus had much higher MR effect than the A-PUS-MRE because the G_0' of the I-PUS-MR was lower. A-PUS-MRE possessed the highest $\Delta G'$, indicating better magnetic field-induced mechanical properties. The topological

Table 1
The mechanical properties of the A-MREs and I-MREs.

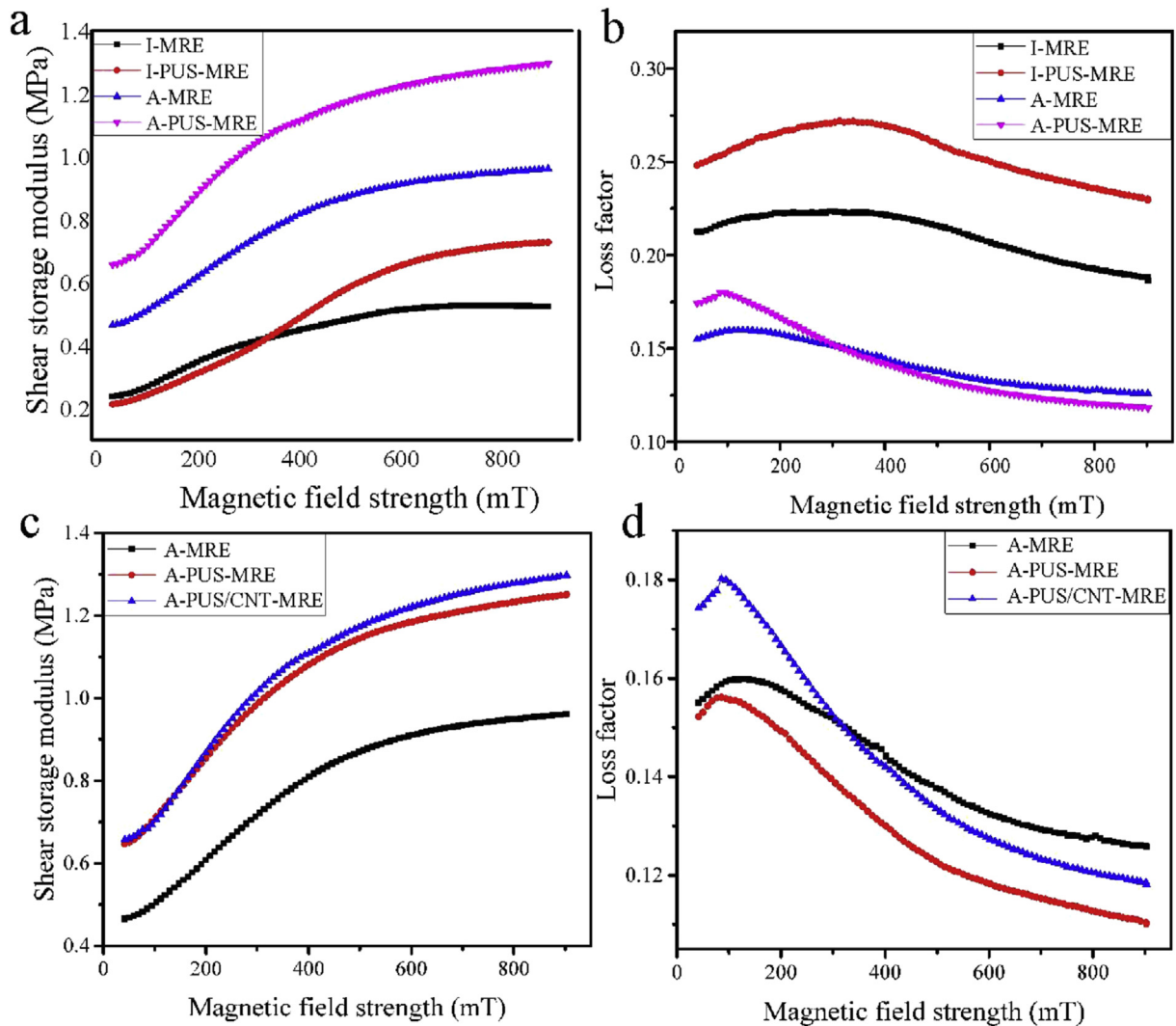|	G_0' (MPa)	G_{max}' (MPa)	$\Delta G'$ (MPa)	MR effect (%)
A-PUS-MRE	0.66	1.30	0.64	97%
A-MRE	0.47	0.96	0.49	104%
I-PUS-MRE	0.21	0.73	0.52	248%
I-MRE	0.24	0.52	0.28	117%

Fig. 2. The influence of porous PUS and CNTs on A-MRE and I-MRE mechanical properties.

confinement helped to form robust alignment of CIPs. The as-prepared A-PUS-MRE possessed highest initial modulus and magnetic induced modulus, indicating that the mechanical properties were improved.

The influence of topological confinement on the loss factor was shown in Fig. 2(b). Generally speaking, the loss factor of all four samples firstly increased slightly with increasing external magnetic field and then decreased because the loss factor came mainly from the sliding friction between the CIPs and matrix, as well as from the interaction between the CIPs when moving under the magnetic field. The initial loss factor of I-MRE was much larger than that of A-MRE because the CIPs in A-PUS-MRE and I-PUS-MRE were anchored to the sponge by PDMS molecular chains. When the magnetic field was applied, CIPs aligned along the magnetic field direction. As compared to the pure PDMS matrix, the sliding fraction and the energy dissipation in the PDMS/PUS matrix should be higher. The loss factor of A-PUS-MRE decreased from 1.18 to 0.12, whereas that of A-MRE decreases from 1.16 to 0.13. Owing to the topological confinement effect, the movement of CIPs in the PUS microstructures was difficult than that in the pure PDMS matrix. Thus the sliding friction between the CIPs and the matrix was much smaller under an applied the magnetic field. That means that the incorporation of topological structures can significantly expand the range of the loss factor by controlling the external magnetic field.

Fig. 2 (c) and (d) show the storage modulus and loss factor of PUS-MRE and PUS/CNT-MRE. In comparison to the PDMS based pure MRE, both the PUS topological confinement and the CNT conductive layer improved the mechanical properties. In Fig. 2(c), The G_{max}' values of the A-PUS-MRE and A-PUS/CNT-MRE were 1.25 MPa and 1.30 MPa, respectively, values that were much larger than that of A-MRE because the G_{max}' value of the A-MRE was only 0.96 MPa. The G_0' of the A-PUS-MRE and A-PUS/CNT-MRE were 0.65 MPa and 0.66 MPa, respectively, whereas that of A-MRE was 0.47 MPa. Because CIPs in MREs were confined into the micro-holes of the PUS, they could not move as easily as in A-MREs. As a result, A-PUS-MRE was strengthened by the sponge. The incorporated sponges not only strengthened the MREs but also increased the $\Delta G'$. The $\Delta G'$ of A-MRE was only 0.49 MPa, whereas that of A-PUS-MRE was 0.65 MPa. However, the CNTs exhibited few effects on increasing the $\Delta G'$ of the MREs. $\Delta G'$ only increased from 0.65 MPa to 0.66 MPa, when the MRE incorporated CNT/PUS instead of PUS.

Fig. 2(d) showed the sponge and the CNT influenced on the loss factor of the MREs. The loss factor of the A-MRE changes from 0.16 to 0.13, while the loss factor of A-PUS-MRE showed a smaller range from 0.15 to 0.11. Because the CIPs were confined to the micro-holes in A-PUS-MRE and thus had more difficulty moving than the free CIPs in A-MRE, the sliding friction between the CIPs and the matrix tend to be smaller. On the other hand, the CNT coated on the PUS increased the sliding friction of the MREs, so the loss factor of the A-PUS/CNT-MRE was larger, and it changed from 0.17 to 0.12.

The mechanical properties of the 3D topological structure enhanced MREs was further systematically investigated by varying CIP content at 40 wt%, 60 wt%, 70 wt% and 80 wt% (Fig. 3). The G_0' of the A-PUS/CNT-MRE increased from 0.23 to 0.37, 0.66 and 1.30 MPa while increase the CIP content, which indicated that the CIPs enhanced the MRE mechanical properties. With increasing strength of magnetic field, the G' increased to 0.33, 0.62, 1.30 and 2.06 MPa gradually. This was because the magnetization of the CIPs increased with increasing of the magnetic field before reaching the magnetic saturation. Meanwhile, the increase in CIPs content decreased the magnetic induced particle-particle distance between two adjacent soft magnetic particles, and thus the interaction between the CIPs was increased. The increased interaction lead to a stronger CIPs linear structure and therefore the increase of G' was mainly caused by the increasing interaction between the magnetic particles.
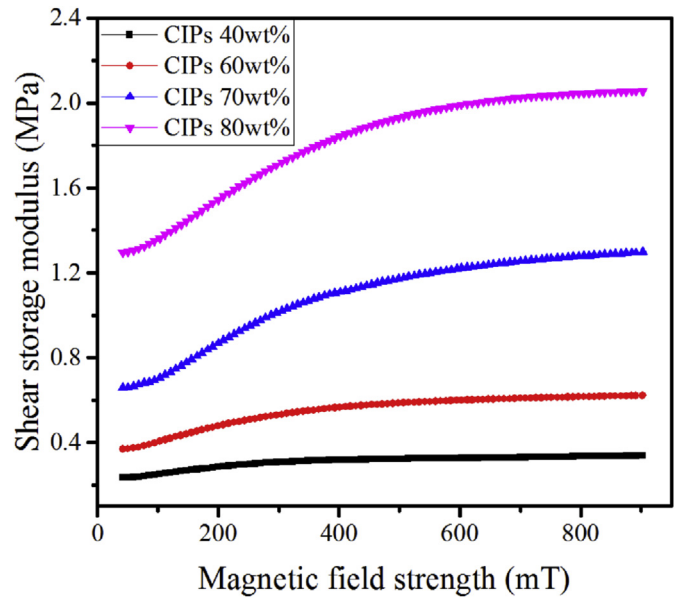

Fig. 3. Shear storage modulus of A-PUS/CNT-MRE with different CIP content under different magnetic field strength.

Fig. 4 shows the tensile variation versus strain of I-PUS/CNT-PDMS-MRE and I-PUS-PU-MRE (70 wt% CIPs). I-PUS/CNT-PDMS-MRE presented obvious three stages during the test including: elastic deformation, plastic deformation and destruction. The samples were typical elastic composites. The elastic deformation of the I-PUS/CNT- PDMS-MRE ranges from 0 to 0.47 and the plastic deformation of the I-PUS/CNT- PDMS-MRE ranges from 0.47 to 0.80. Finally, the sample was broken when the strain was larger than 0.80. From the tensile test, we found that the I-PUS/CNT-PDMS-MRE had large elastic and plastic deformation, because the I-PUS-PU-MRE was destroyed when the tensile strain was less than 0.4 in our previous work [33]. Thus, I-PUS/CNT- PDMS-MRE could bear larger tensile strain than I-PUS-PU-MRE. To this end, the elastic I-PUS/CNT- PDMS-MRE was found to be a good candidate for tensile change devices.
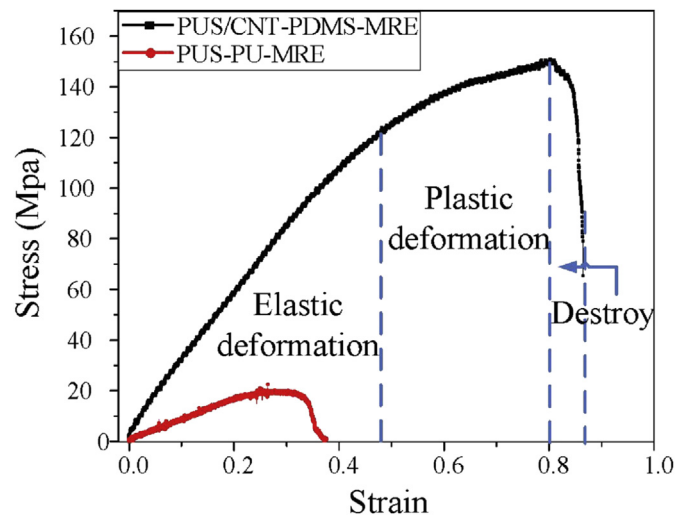

Fig. 4. Tensile variation with strains of the I-PUS/CNT-PDMS-MRE and I-PUS-PU-MRE.

3.2. CNT doped MRE strain sensor

The fabrication process of the strain sensor was illustrated in Fig. 5(a). A highly conductive CNT/PUS was fabricated through a solution-immersion process by dip-coating CNT onto the backbone of the PUS. First, bare PUS was dipped into the 1.2 mg/ml CNT ink and dried in an oven for 30 min. The white PUS turned black when coated with the CNTs. The SEM images (Fig. 5(b), (c), (d)) demonstrate that the conductive CNTs were attached to the surface of the porous sponge. A copper wire was connected to the conductive PUS with the conductive silver adhesives. The conductive CNT/PUS was immersed into the MR precursor. After that, the beaker containing the MR precursor and CNT/PUS was transferred into a vacuum oven and pumped for 30 min to ensure the CNT/PUS being fully filled with MR precursor under the capillary action. Then CNT/PUS filled with MR precursor was transferred into a 100 mm × 100 mm × 2 mm mold and heated for 20 min at 100 °C. Finally, the strain sensor was fabricated. When the strain sensor was stretched, the CNTs coated on the sponge started to separate from each other. As a result, the resistance of the CNT electrode inserted in to the MRE sample changed.

The cycle ability was very important for the strain sensor. Fig. 6(a) depicted the resistance variation of the strain sensor during stretch/release cycles. It was found that the resistance of the strain sensor could return to 27.5 kΩ during five cyclic loading cycles, so the strain sensor had superb elasticity and resilience. Fig. 6(b) shows the cyclic loading strain on the conductive MRE samples, where the cyclic loading increased the strain gradually to 0.5 and then decreased at the rate of 100 mm/min. The resistance of the MRE increased with increasing tensile strain, and range from 27.5 kΩ to 30.5 kΩ. The response of MRE resistance (Fig. 6(a)) was proportional to the applied strains, and the resistance variation tendency coincided with each other at

five cycles. The conductive MRE possessed both high stretchability and sensitivity, which made it an ideal candidate for strain sensor.

The resistance responses of I-PUS/CNT-MRE to repeat extension loading and unloading cycles were recorded and plotted in Fig. 7. The strain sensor resistance increased with increasing transverse loading force, whereas the resistance changes of the different loops were quite similar, which indicated that the electromechanical changes were quite stable at different cycles. In addition, the resistance changes with different extension rates were investigated, and the tensile rate of cycle tensile loading test on the strain sensor was 50 mm/min, 100 mm/min, 150 mm/min, 200 mm/min, 250 mm/min and 300 mm/min. The consistent resistance varied with the stretching force on the sample, and it was maintained under different extension rate, which proved the reliability of I-PUS/CNT-MRE as a strain sensor.

4. Conclusion

In summary, a novel conductive MRE consisting PDMS, porous PUS, CNTs and CIPs was fabricated. Owing to the enhancing effect of the porous 3D continues structure, the MR effect and magnetic induced modulus of the MRE were significantly improved. The magnetic saturation modulus of A-MRE with sponge was 1.30 MPa when CIPs content was 70 wt%. The MR effect of A-MRE and A-PUS-MRE decreased from 104% to 97.0% and the magnetic induced modulus had increased from 0.49 MPa to 0.64 MPa. The high sensitive and low cost MRE tensile sensor can maintain consistent resistance with various stretching forces under different extension rates. This work provided a new way to design and improve the properties of the MREs. The final products have significant potential in terms of applying them to sensors.
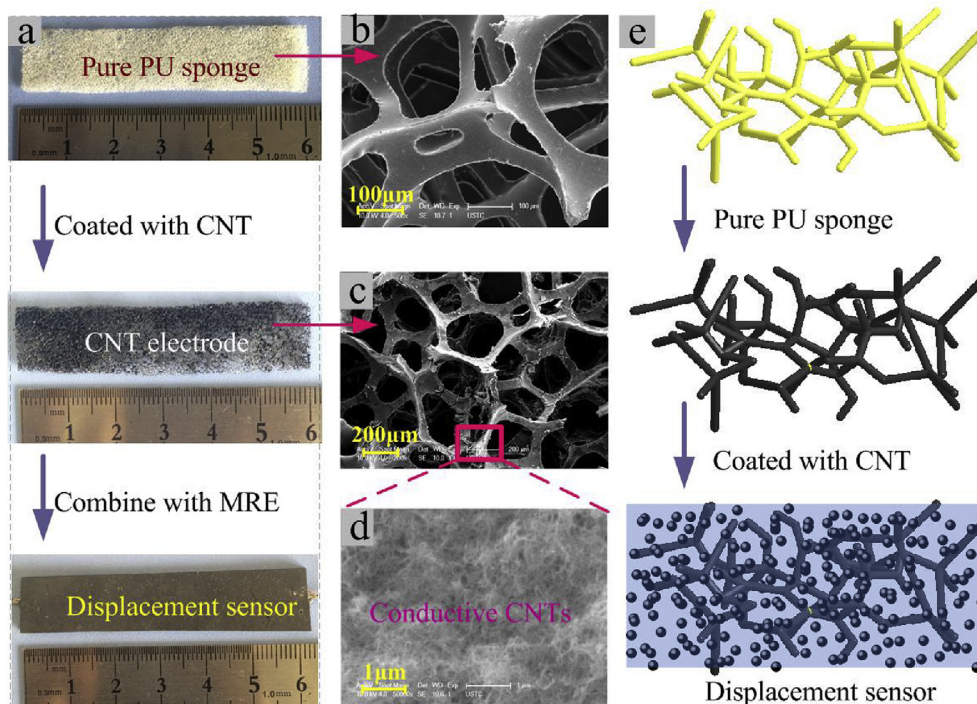

Fig. 5. Fabrication of the strain sensor (a) Optical images of the pure porous CNT/PUS electrode and the strain sensor. (b) SEM images of the pure PUS. (c) SEM images of the CNT electrode. (d) Magnification of sponge surface with CNT covered. (e) Schematic illustration of the fabrication processes of the strain sensor.
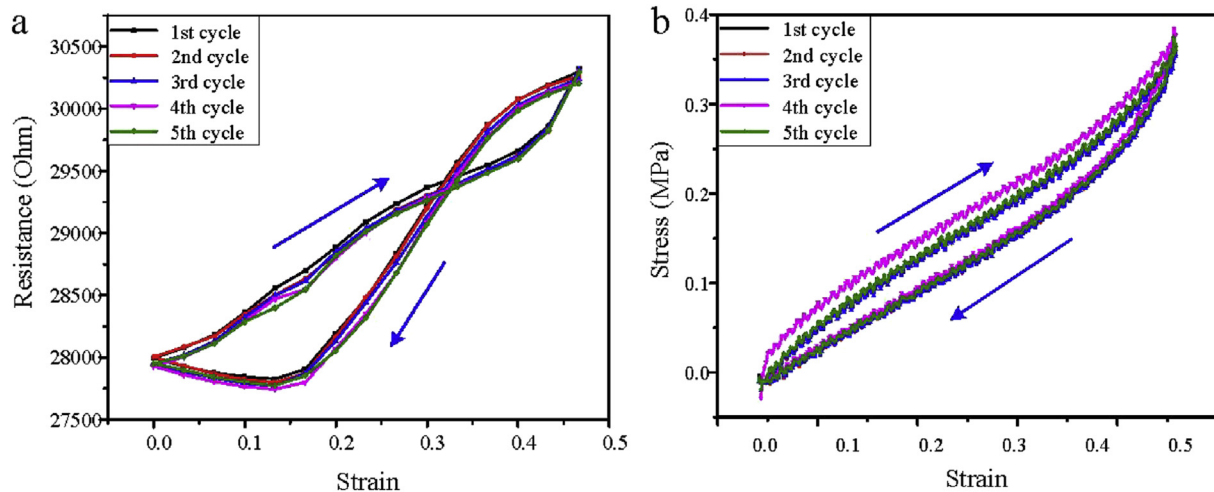
Fig. 6. Changes in relative resistance under 50% strain stretch/release cycles. a) The cyclic resistance changes with strain and b) Cyclic loading strain on the strain sensor.
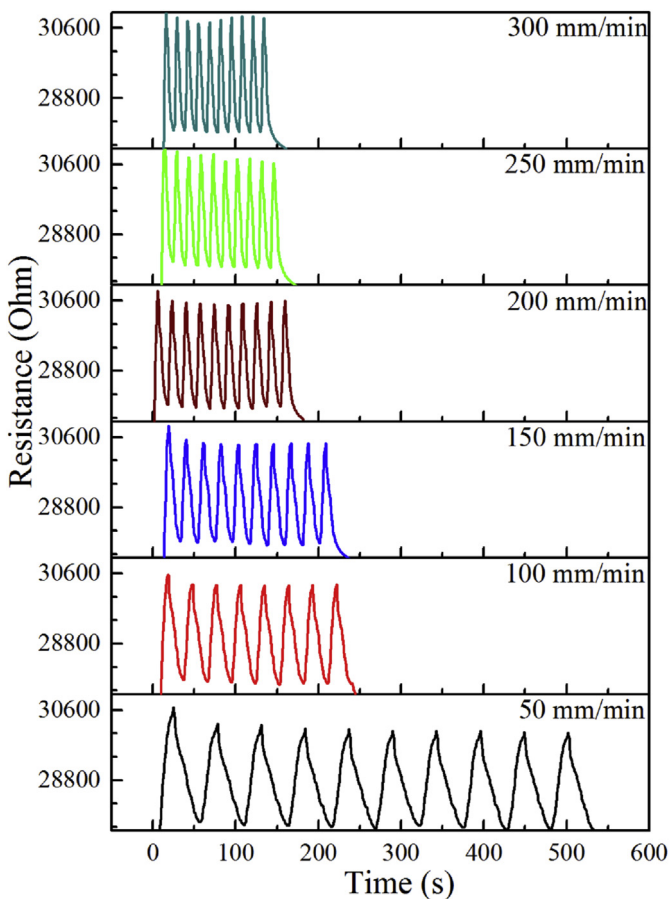

Fig. 7. Resistance change of the sensor unit as a function of time at incrementally increasing and decreasing displacement (0–20 mm) at different tensile rate.

References

[1] S.S. Sun, J. Yang, H.X. Deng, H.P. Du, W.H. Li, G. Alici, M. Nakano, Horizontal vibration reduction of a seat suspension using negative changing stiffness magnetorheological elastomer isolators, Int. J. Veh. Des. 68 (2015) 104–118.

[2] P. Blom, L. Kari, The frequency, amplitude and magnetic field dependent torsional stiffness of a magneto-sensitive rubber bushing, Int. J. Mech. Sci. 60 (2012) 54–58.

[3] R. Sinko, M. Karnes, J.H. Koo, Y.K. Kim, K.S. Kim, Design and test of an adaptive vibration absorber based on magnetorheological elastomers and a hybrid electromagnet, J. Intel. Mat. Syst. Str. 24 (2012), 1045389X12463461.

[4] J.D. Carlson, M.R. Jolly, MR fluid, foam and elastomer devices, Mechatronics 10 (2000) 555–569.

[5] C. Bellan, G. Bossis, Field dependence of viscoelastic properties of MR elastomers, Int. J. Mod. Phys. B 16 (2002) 2447–2453.

[6] G. Zhou, Shear properties of a magnetorheological elastomer, Smart. Mater. Struct. 12 (2003) 139–146.

[7] B. Salskia, W. Gwarek, P. Korpas, S. Reszewicz, A. Chong, P. Theodorakeas, I. Hatziioannidis, V. Kappatos, C. Selcuk, T.H. Gan, M. Koui, M. Iwanowski, B. Zielinski, Non-destructive testing of carbon-fibre-reinforced polymer materials with a radio-frequency inductive sensor, Compos. Struct. 122 (2015) 104–112.

[8] J. Gerard Gallo, T.Erik Thostenson, Spatial damage detection in electrically anisotropic fiber-reinforced composites using carbon nanotube networks, Compos. Struct. 141 (2016) 14–23.

[9] G. Yu, M.Q. Zhang, H.M. Zeng, H.B. Zhang, Conductive polymer blends filled with carbon black: positive temperature coefficient behavior, Polym. Eng. Sci. 39 (1999) 1678–1688.

[10] Y.H. Huang, Y.H. Jiang, X.B. Yang, H.Y. Sun, H.G. Piao, R.Z. Xu, Enhanced conductivity of magnetorheological fluids based on silver coated carbonyl particles, J. Mater. Sci. Mater. Electron 27 (2016) 255–259.

[11] T.F. Tian, W.H. Li, Y. Deng, Sensing capabilities of graphite based MR elastomers, Smart. Mater. Struct. 20 (2011) 025022.

[12] X. Li, X.Y. Ma, Y.F. Feng, L. Wang, C.T. Wang, A novel composite scaffold consisted of porous titanium and chitosan sponge for load-bearing applications: fabrication, characterization and cellular activity, Compos. Sci. Technol. 117 (2015) 78–84.

[13] V. Birman, K. Chandrashekhara, M. Hopkins, J.S. Volz, Effects of nanoparticle impregnation of polyurethane foam core on the performance of sandwich beams, Compos. B. Eng. 46 (2013) 234–246.

[14] J. Perlich, G. Kaune, M. Memesa, J.S. Gutmann, P. Müller-Buschbaum, Sponge-like structures for application in photovoltaics, Philos. T. R. Soc. A 367 (2009) 1783–1798.

[15] L.M. Li, C.H. Zhu, Y.P. Wu, J.H. Wang, T.L. Zhang, Y. Liu, A conductive ternary network of a highly stretchable AgNWs/AgNPs conductor based on a polydopamine-modified polyurethane sponge, RSC Adv. 5 (2015) 62905–62912.

[16] H.B. Yao, J. Ge, C.F. Wang, X. Wang, W. Hu, Z.J. Zheng, A flexible and highly pressure sensitive graphene–polyurethane sponge based on fractured microstructure design, Adv. Mater. 25 (2013) 6692–6698.

[17] Y. Liu, J.K. Ma, T. Wu, X.R. Wang, G.B. Huang, Y. Liu, H.X. Qiu, Y. Li, W. Wang, J.P. Gao, Cost-effective reduced graphene oxide-coated polyurethane sponge as a highly efficient and reusable oil-absorbent, ACS Appl. Mater. Inter 5 (2013) 10018–10026.

[18] G. Toulouse, M. Kléman, Principles of a classification of defects in ordered media, J. Phys. Lett. 37 (1976) 149–151.

[19] A. Golemme, S. Zumer, D.W. Allender, J.W. Doane, Continuous nematic-

isotropic transition in submicron-size liquid-crystal droplets, Phys. Rev. Lett. 61 (1988) 2937—2940.

[20] E. Terentjev, Disclination loops, standing alone and around solid particles, in nematic liquid crystals, Phys. Rev. E 51 (1995) 1330—1337.

[21] X.L. Wu, W.L. Goldburg, M.X. Liu, J.Z. Xue, Slow dynamics of isotropic-nematic phase transition in silica gels, Phys. Rev. Lett. 69 (1992) 470—473.

[22] L.L. Li, W.T. Duan, Q. Yuan, Z.X. Li, H.H. Duan, C.H. Yan, Hierarchical c-Al2O3 monoliths with highly ordered 2D hexagonal mesopores in macroporous walls, Chem. Commun. 10 (2009) 6174—6176.

[23] C.F. Wang, S.J. Lin, Robust superhydrophobic/superoleophilic sponge for effective continuous absorption and expulsion of oil pollutants from water, Appl. Mater. Interfaces 5 (2013) 8861—8864.

[24] B. Ge, Z.Z. Zhang, X.H. Men, X.Y. Zhou, Q.J. Xue, A graphene coated cotton for oil/water separation, Compos. Sci. Technol. 102 (2014) 100—105.

[25] W. Chen, R.B. Rakhi, L.B. Hu, X. Xie, Y. Cui, H.N. Alshareef, High-performance nanostructured supercapacitors on a sponge, Nano. Lett. 11 (2011) 5165—5172.

[26] L.R. Lakshman, K.T. Shalumon, S.V. Nair, R. Jayakumar, S.V. Nair, Preparation of silver nanoparticles incorporated electrospun polyurethane nano-fibrous mat for wound dressing, J. Macromol. Sci. A 47 (2010) 1012—1018.

[27] P. Ang-atikarnkul, A. Watthanaphanit, R. Rujiravanit, Fabrication of cellulose nanofiber/chitin whisker/silk sericin bionanocomposite sponges and characterizations of their physical and biological properties, Compos. Sci. Technol. 96 (2014) 88—96.

[28] F. Ji, C.L. Li, B. Tang, J.H. Xu, G. Lu, P. Liu, Preparation of cellulose acetate/zeolite composite fiber and its adsorption behavior for heavy metal ions in aqueous solution, Chem. Eng. J. 209 (2012) 325—333.

[29] A. Bayat, S.F. Aghamiri, A. Moheb, G.R. Nezhaad, Oil spill cleanup from sea water by sorbent materials, Chem. Eng. Technol. 28 (2005) 525—528.

[30] Q. Zhu, Q.M. Pan, F.T. Liu, Facile removal and collection of oils from water surfaces through superhydrophobic and superoleophilic sponges, J. Phys. Chem. C 115 (2011) 17464—17470.

[31] S. Wang, S.H. Xuan, W.Q. Jiang, W.F. Jiang, L.X. Yan, Y. Mao, M. Liu, X.L. Gong, Rate-dependent and self-healing conductive shear stiffening nanocomposite: a novel safe-guarding material with force sensitivity, J. Mater. Chem. A 3 (2015) 19790—19799.

[32] D. Günther, D.Y. Borin, S. Günther, S. Odenbach, X-ray micro-tomographic characterization of field-structured magnetorheological elastomers, Smart. Mater. Struct. 21 (2012) 015005.

[33] L. Ge, S.H. Xuan, G.J. Liao, T.T. Yin, X.L. Gong, Stretchable polyurethane sponge reinforced magnetorheological material with enhanced mechanical properties, Smart. Mater. Struct. 24 (2015) 037001.